Experimental and numerical assessment of thermal fatigue in 316 austenitic steel pipes

Elena Paffumi[1] and Karl-Fredrik Nilsson

European Commission, DG-JRC, Institute for Energy and Transport, [1] via Fermi 2749, 21027, Ispra Italy, [2]1755 ZG, Petten, The Netherlands,

[1]elena.paffumi@jrc.ec.europa.eu, [2]karl-fredrik.nilsson@jrc.nl,

Keywords: thermal fatigue, creep-fatigue, TOFD, elastic-plastic fracture, elastic fracture, 316L austenitic steels

Abstract. This paper presents an experimental and numerical investigation of 316L steel pipe components with 14 mm wall thickness heated by induction to 300 – 550 ˚C on the outer surface and cyclically cooled with room temperature water. The damage is initiated as network of surface cracks where some cracks become dominant. At 550˚C the pipe fails after typically 50 000 cycles whereas at 300˚C the deepest cracks have only penetrated half the thickness after 250000 cycles. By applying a small axial load the deepest cracks switch from axial to circumferential. An elasto-plastic fatigue model was adopted to simulate the crack propagation. The difference in crack propagation rate and fatigue life when the temperature is increased is well captured by the model, but the agreement with tests depends on the fatigue growth parameters. Lower bound values from give very good agreement whereas data from RCC-MRx predict faster crack growth than observed in the tests.

Introduction

Components in nuclear power plants are subjected to thermal fluctuations and mechanical loads. When a surface is subjected to a thermal down-shock the surface layer goes into tension as it attempts to contract against the remaining material. The thermal stresses are self-equilibrating so other parts will be in compression. An up-shock gives a corresponding compression at the surface. The resulting strain and associated stress distributions across the thickness for thermal fatigue are quite complex and depend on the amplitude and frequency of thermal fluctuations and the material properties, where high thermal expansion coefficient and low thermal conductivity promote high surface stresses and strong gradients. Thermal fatigue damage is typically initiated as a network of surface cracks. Depending on the loading and geometry cracks may arrest at a specific depth or propagate to form a through-wall crack. At JRC we have developed a test facility to simulate realistic thermal fatigue loadings and damage evolution in pipe components [1,2]. In parallel we have also developed models with different levels of complexity to assess the initiation of thermal fatigue damage and propagation of thermal fatigue cracks. In the past tests have been performed for pipe components of 316L austenitic steel heated to 300°C, which is representative for light-water reactors. Components in fast reactors (e.g. sodium fast reactors) operate at a typical temperature of 550°C for which creep effects may become important and we have therefore recently also performed tests at this temperature. This paper summarizes the experimental findings with the emphasis on the role of axial load and difference by increasing temperature. The paper also presents some engineering models.

Experimental Programme

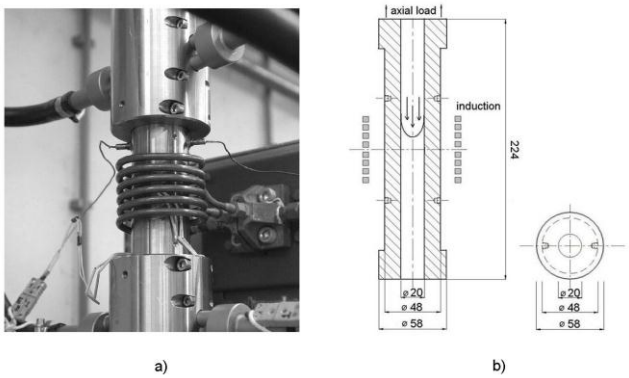

Figure 1 Experimental set-up a) specimen with induction coil b) specimen dimensions.

Figure 1 shows the experimental set-up and specimen geometry. The outer surface is heated by induction to a constant temperature that range from 300 to 550°C, while the inner bore is subjected to repeated quenchings with room temperature water for 5 seconds. The water flow is stopped and the pipe is heated up by conduction from the hot outer surface for 40-45 seconds. The pipe is held in a lever arm test machine that provides a constant axial load but no restraint on axial displacement. The tests are interrupted at different intervals to allow monitoring of defects by surface replicas for shallow defects and time-of-flight diffraction (TOFD) for deeper defects. A network of shallow cracks was detected after a relatively small number of cycles. This is identified as crack initiation. The TOFD measures crack depths and was adopted to monitor crack growth. Table 1 summarizes the test conditions and key features for crack evolution.

Table 1: Thermal fatigue tests summary

Test	t_{Quench} /t_{Heat} [sec]	T_{max} [ºC]	T_{water} [ºC]	ΔT_{in} [ºC]	Axial force [kN]	Crack initiation N_i ×1000	Number of cycles ×1000	Max crack [mm] depth/Failure Circ	axial
TF1	5/40	300	25	~170	-	≤56	256	3.8	4.3
TF2	5/45	400	25	/	-	15-20	47	2.2	6.1
TF3	5/45	350	25	/	-	15-20	30	1.4	1.7
TF4	5/45	300	25	~170	50	<10	250	6.2	3.7
TF6	5/45	300	25	~170	100	≤10	30	1.6	1.2
TFR1	5/45	550	25	~300	-	≤10	46	5.8	Failure
TFR2	5/45	550	25	~300	50	≤10	58	Failure	7.2
TFR3	5/45	550	25	~300	-	≤10	90	7.4	Failure
TFR4	5/45	550	25	~300	50	≤10	50	11	4.7

The axial force 50 and 100 kN give an axial stress for uncracked specimen of 33 and 66 MPa respectively. The temperature variation on the inner surface (ΔT) depends on the temperature of the water and outer surface of the pipe, the duration of the quenching and heating and the heat transfer between the water and the pipe. It was not possible to measure ΔT at the inner surface in a reliable way. The values in Table 1 were derived from a calibration specimen with six thermocouples across the wall thickness calibrated with analytically computed transient temperature distributions.

Main Experimental observations

The typical network of surface cracks was detected in all tests. For TF1, the first replica test was performed after 56 000 cycles but crack initiation happened well before. For the other tests the first replica was taken after 10 000 cycles or less. A large number of axial and circumferential cracks were observed by the TOFD measurements. The TOFD technique only measures crack depth, a, but aspect ratios between crack depth and crack length, $2c$, were checked by cutting some specimens. In general the crack aspect ratio increased with crack depth. The evolution of the cracks was very

complex. There was a large number of axial and circumferential cracks that interact in a complex way so that crack propagation rate varied between cracks with similar crack depth and individual defects could both increase and decrease growth rates with increasing depth. The stress from the axial load is small compared to the thermal stresses and did not increase the rate of deepest crack. The axial load increased however the number of circumferential cracks substantially as shown in Figure 2. Axial cracks tended to be deeper when there is no axial force, whereas with axial load the deepest cracks were circumferential, Figure 3a, 3b and Table 1.

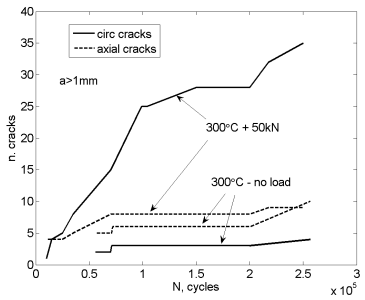

Figure 2 Measured number of axial and circumferential cracks larger than 1 mm vs. number of cycles at 300 C (TF1 and TF4) ;

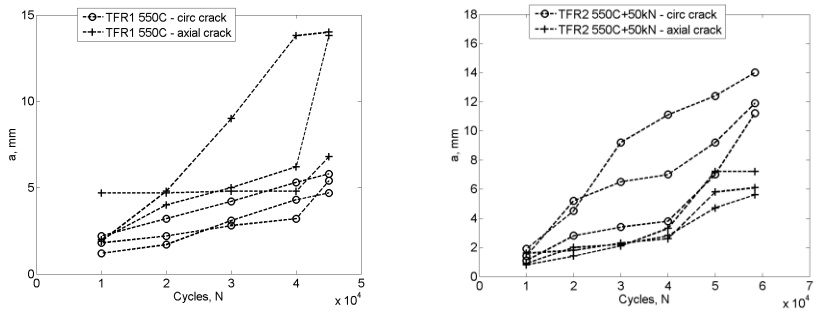

Figure 3 Measured crack depth of leading cracks vs. number of cycles at 550 C a) TFR1 no axial load b) TFR2 axial load 50 kN

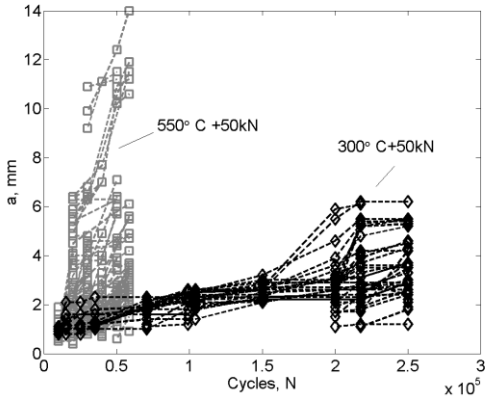

Figure 4 Crack depth vs. number of cycles for the tests with axial load 50 kN TF4 300°C, TFR2 550°C

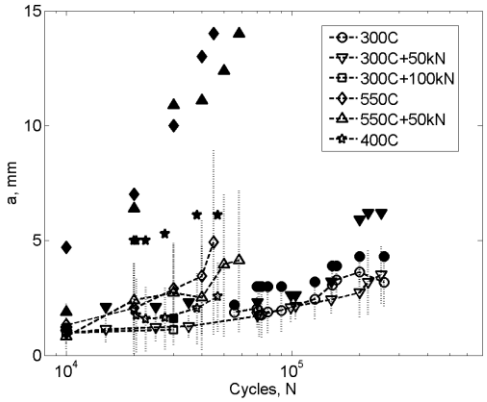

Figure 5 Measured crack growth data; mean value (open symbol with dotted line); standard deviation (vertical line) and maximum value (filled symbol)

There were no through-cracks for the tests with outer surface temperature 300 or 400 ºC. For the higher temperature (550°C), a lead crack propagated through the wall and the component failed. Figure 4 depicts the measured crack depths vs. the number of cycles for tests with axial load. The higher crack growth rate at 550 °C is clearly seen. Figure 5 depicts the mean value, one standard deviation and the maximum value of the crack depth for tests TF1, TF4, TF2, TFR 1 and TFR2. It can be noted that the axial load has a very small effect at both 300 and 550°C. The higher temperature increases the mean value of the crack depth and the deepest outgrow the other cracks. Figure 6 shows TFR1 and TFR2 after failure with axial and circumferential through-wall defect respectively. Figure 7 shows one axial defect at the inner surface that interacts with small circumferential cracks. Such interaction may promote temporary crack arrest, which could be one reason for the variation in crack propagation rate seen in the tests.

a) b)

Figure 6 Failed component a) TFR1 with axial crack b) TFR2 with circumferential crack

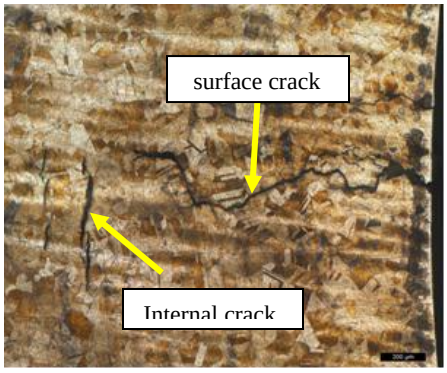

Figure 7 Surface breaking axial crack interacting with embedded circumferential cracks

Modelling of the tests

The thermal fatigue tests presented above simulate many coupled features that are observed in real components but are very difficult to include in an analysis. These include: complex heat transfer between the cold fluid and the hot pipe; a complex and time dependent through-wall distribution of temperature and resulting stresses and strains; deformation by cyclic plasticity; a large number of interacting axial and circumferential cracks; temperature dependence of material properties (cyclic stress-strain curves, fatigue propagation data and creep properties). It is obvious that we need to introduce a number of simplifying assumptions.

Distribution of temperature and resulting stresses and strains for uncracked body

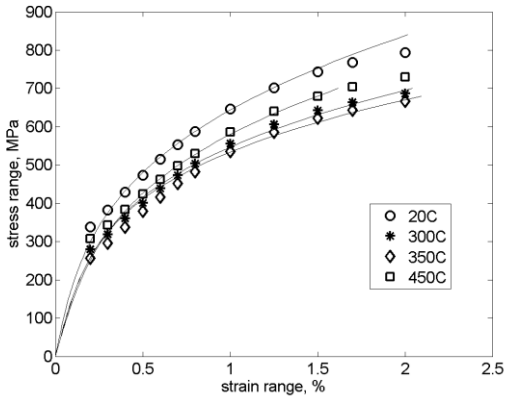

Figure 8 cyclic stress-strain curve for 316L stainless steel (solid lines RCC-M and symbols model used in analysis)

The distribution of the temperature and resulting strains and stresses were done by an ABAQUS finite element analysis with axisymmetric elements with a rather fine mesh at the inner surface to capture the gradients. The temperature distribution was first computed by a thermal analysis. At the inner surface heat flux from a heat transfer coefficient and the temperature difference between the inner surface and the surrounding media (25°C) was imposed. At the outer surface the constant temperature was imposed (300 or 550º C). Heat transfer in the pipe was by linear conduction. Temperature dependent heat transfer coefficients water/solid and air/solid were derived from basic formulae. This computed ΔT at the inner surface was higher than the values reported in Table 1. The stresses and strains were computed from the temperature distributions imposed on an uncracked cylinder. The physical and mechanical properties (e.g. thermal conductivity, E-modulus, thermal expansion coefficient, cyclic stress-strain curve) were taken from the French RCC-M code with appropriate temperature dependence [4]. The thermal loads are sufficient to infer cyclic plastic deformation in the pipe. To this end a stabilized kinematic hardening Chaboche model was adopted, $\Delta\sigma = 2\sigma_o + 2C_H / \gamma(1-e^{-\gamma\Delta\varepsilon_{pl}})$, where σ_0, is the cyclic yield stress, and C_H and γ are characteristic coefficients of the material. Figure 8 shows the cyclic stress curve from RCC-M and the corresponding curves for the model with calibrated parameters. Figure 9a and 9b show the computed stress and strain range distributions during one cycle for the 300 ºC case

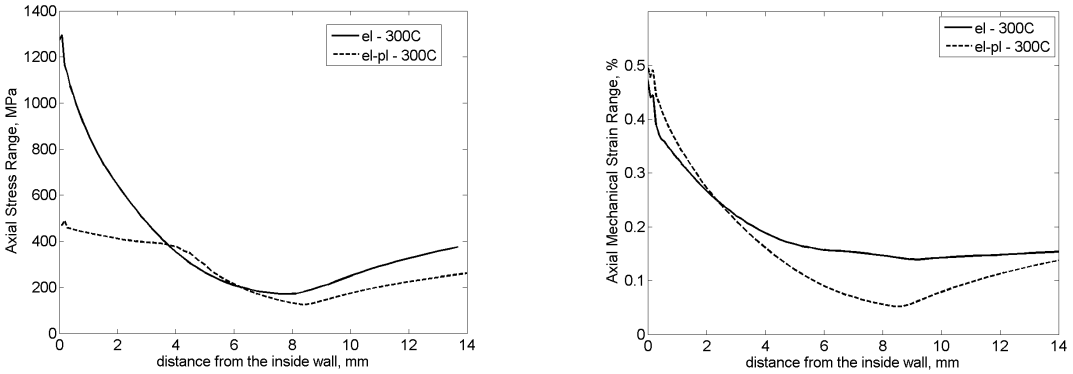

a) b)

Figure 8 Resulting distribution of a) stress range b) mechanical strain range for 300 ˚C and F = 0.

Crack Propagation

Crack initiation can be reasonably predicted from the computed strain distributions and fatigue curves [1]. In this paper we concentrate on crack propagation. We assume that there is cyclic dependent fatigue crack growth governed by Paris law. To this end we need to compute the crack growth parameters. For a linear elastic analysis it is possible to compute the stress intensity factor for a semi-elliptical crack in a cylinder and a given stress distribution. The stress distribution is fitted to a polynomial $\sigma = b_0 + b_1 x/t + b_2 (x/t)^2 + b_3 (x/t)^3$, where x is the distance from the inner surface and t the wall thickness. The stress intensity factor is then computed from,

$$K = \sqrt{\pi a / Q}\left[b_0 i_0 + b_1 i_1 x/t + b_2 i_2 (x/t)^2 + b_3 i_3 (x/t)^3\right], \quad (1)$$

where i_0, i_1, i_2 and i_3 are influence coefficients that depend on the crack/thickness ratio, a/t, on the shape of the crack, a/c, and on the location along the crack front, e.g. [3]. Q is a shape correction factor, and for a semi-elliptical crack $Q = 1 + 1.464(a/c)^{1.65}$. The thermal loads in our case will give plastic deformation and since thermal loads correspond to displacement controlled conditions, a linear elastic analysis will be very conservative as seen be the higher elastic stresses in Figure 9. Here we will compute a "plastic stress intensity factor" as follows. First a stress intensity factor, K_{pl}, is computed from Eq. (1) using the stress distribution from the elasto-plastic analysis. The crack opening displacement for a prescribed stress is however higher due to yielding and we account for this by multiplying with a crack tip opening displacement factor derived from a yield strip model $\delta_{pl}/\delta_{el} = \sqrt{8(\sigma_Y/\sigma_\infty \pi)^2 \, ln(sec(\pi\sigma_\infty / 2\sigma_Y))}$. σ_Y is the yield stress and σ_∞ the mean stress along a segment corresponding to the crack length. Hence the corresponding plastic K is $K_{pl} \cdot \sqrt{\delta_{pl}/\delta_{el}}$. A corresponding J-integral would be $J = K_{pl}^2 \cdot \delta_{pl}/\delta_{el}/E^*$. The plasticity correction is rather sensitive to the value of the yield stress. In the analysis we used the mean value of initial yield and ultimate strength from the cyclic plasticity curve. We assume cyclic crack propagation controlled by Paris law,

$$(da/dN)_f = C_P(\Delta K_{eff})^{m_P} \quad (2)$$

For consistency the RCC-MRx data are used [4]. At 300°C, $C_p = 7.5 \cdot 10^{-10}$ and 4 for n_p with K in MPa√m and a in *mm*. The Paris law parameters found in the literature vary and the RCC-MRx give quite high rates. Previously we have used $C_p = 2.7 \cdot 10^{-10}$ and m_p= 3.89 [5], which gives four times lower crack growth rate. For a given crack geometry (a and c) and stress distribution, the stress

intensity factor can be computed as function of time. The stress intensity range, ΔK, is computed from the maximum and minimum value during each cycle. A negative K is interpreted as crack closure and in that case the minimum K during the cycle is zero. In our case the minimum K was negative so ΔK_{eff} was equal to the maximum K. The stress intensity factor depends on the crack aspect ratio. We know from experiments that the crack aspect ratio increases with crack depth. For very shallow cracks it could be close to unity and for a through-wall crack it is typically 15. This can be simulated by choosing the aspect ratio which gives equal stress intensity factor at the deepest point and at one point along the semi-elliptical crack front close to the free surface.

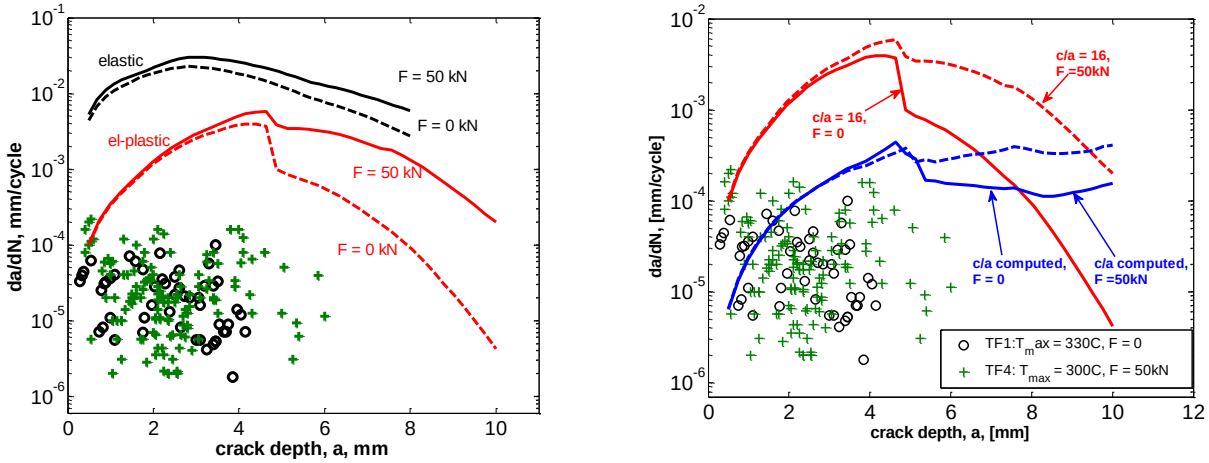

Figure 10 Computed and measured crack growth rates a) elastic and elasto-plastic analysis with c/a = 16 b) elasto-plastic analysis with c/a = 16 and c/a computed.

Figure 10 shows the computed growth rates for circumferential cracks vs. crack depth with and without axial load together with experimental values. The experimental values are taken form measured crack depths at two intervals from TOFD and divided by the number of cycles in the interval. In Figure 10a the computed curves are based on elastic and elasto-plastic analysis as outlined above and with a fixed aspect ratio. In Figure 10b the elasto-plastic model is used but with aspect ratio fixed and computed as outlined above. It follows immediately from Figure 10a that an elastic analysis gives a significantly higher crack growth rate and that the elasto-plastic model predictions agree better with the experimental data. As seen in Figure 10b, predictions are closer to experimental data when the aspect ratio is computed rather than assuming a high fixed value. Nevertheless it is still a bit higher than test data, which could be due to conservatism in the RCC-MRx fatigue data. The model with varying aspect ratio predicts an increasing aspect ratio for increasing crack depth. For cracks with depth below 5 mm *a/c* is around 2 and then it increases drastically. The lower aspect ratio is the reason for the lower crack growth rate for the variable aspect ratio with shallow cracks. For short cracks (< 1mm) Paris law is expected to underestimates the crack propagation rate. The axial load gives only a marginal contribution to the crack growth. This axial load effect is smaller for the case with varying aspect ratio since the axial load effect is compensated by a reduced aspect ratio. The crack propagation rate for axial cracks is not shown but they are very similar to the circumferential cracks.

Below 450°C creep effects are negligible for 316L and we therefore expect no time dependence or creep effect at 300°C. When the pipe is heated to 550 °C creep may have an effect. From the experiments we know that the crack growth rate was significantly higher when the outer surface temperature was increased from 300°C to 550°C and that the pipes failed. One obvious reason is that the thermal loads are much higher (the estimated ΔT from thermocouple readings increases

from 170°C to 300°C). This effect is included in our assessment. For the parameters C_p and m_p in Paris law, there is very weak temperature dependence between room temperature and 350°C. Above 350°C there is a significant effect and the crack growth rate at 550°C is typically 2-10 times higher for the same ΔK [6]. The RCC-MRx gives $C_p = 5 \cdot 10^{-8}, n_p = 3.3$ at 550 ºC, which gives a increase in the crack growth rate by a factor 12, 6 and 4 compared to 300 °C for ΔK = 10, 30 and 60 $MPa\sqrt{m}$. It is straightforward to modify the Paris law accordingly in the analyses but as the temperature varies during the cycle it is not so obvious which value to use. Using the maximum temperature for the entire cycle and through the whole thickness would give a conservative estimate. Finally there may also be a real time dependent effect. In that case it is customary to split the crack growth into a cyclic part and a time dependent part

$$da/dN = (da/dN)_f + (da/dN)_c \quad . \tag{3}$$

The cyclic part is governed by Paris law Eq (2) whereas the "creep" crack growth rate is assumed to be governed by a C(t) integral and the propagation over a cycle is then computed by integration of the duration of one cycle.

$$da/dt = A \cdot C(t)^q, \quad da/dN = \int^T A \cdot C(t)^q d\tau \tag{4}$$

For 316L, $A = 8.05 \cdot 10^{-2}$ and q = 0.81 when C(t) is measured in N/mm/h and da/dt in mm/h [4]. No global creep is expected and creep is not included in the global finite element analysis. At the crack tip stresses are high and creep deformation may take place. For the creep deformation we also follow the RCC-MRx with a primary and secondary creep contribution,

$$\left.\begin{aligned} &\varepsilon_{pc} = C_1 t^{C_2} \sigma^{n_1} \text{ and } \dot{\varepsilon}_{pc} = K \varepsilon_{pc}^{x} \sigma^{y}, \quad t < t_{pc} \text{ where } t_{pc} = \left(c/(C_1 C_2)\right)^{1/(C_2-1)} \cdot \sigma^{(n-n_1)/(C_2-1)} \\ &\varepsilon_{sc} = \varepsilon_{pc}(t = t_{pc}) + C\sigma^n (t - t_{pc}) \text{ and } \dot{\varepsilon} = C\sigma^n \ t > t_{pc} \end{aligned}\right\} \tag{5}$$

The parameters C_1, C_2, n_1, C and n depend on the temperature and values are given in [4]. The C(t) depends on the extension of the creep zone and may be formally written as $C(t) = C_{pc}(t) + C_{sc}(t) + C^*$ [7], where C* is the steady-state large scale creep and $C_{pc}(t)$ $C_{sc}(t)$ the small scale primary and secondary creep. Estimates of $C_{pc}(t)$ and $C_{sc}(t)$ and corresponding crack growth per cycle through integration is:

$$\left.\begin{aligned} &C_{sc}(t) = \frac{J}{\Omega \cdot t} \Rightarrow \left(da/dN\right)_{pc} = A(J/\Omega)^q \cdot T^{1-q}/(1-q), \Omega = (1-x) \cdot (y/(1-x)+1)^{1/(1-x)} \\ &C_{sc}(t) = \frac{J}{(n+1) \cdot t} \Rightarrow \left(da/dN\right)_{sc} = A[J/(n+1)]^q \cdot T^{1-q}/(1-q) \end{aligned}\right\} \tag{6}$$

The time when primary creep ends depends on the stress and the temperature. Using the data in [4] the time for primary creep, t_{pc}, at 550ºC is much longer that the period of the cycle. Hence there should be no steady-state creep and the contribution from C* should be smaller than from primary and secondary creep. The contribution to da/dN from the primary and secondary creep at 550 °C estimated from Eq. (6) is much smaller than the cyclic fatigue contribution. Hence the creep contribution is negligible.

Figure 11 and 12 show the computed crack growth ratio vs. crack depth and crack depth vs. number of cycles together with experimental data. The computed use the elasto-plastic model with computed crack aspect ratio. We note that the computed crack growth rates are significantly higher than the measured data. This is quite likely due to the high crack growth rate values in RCC-MRx. The difference between RCC-MRx and [5] is a factor 4 at 300 °C. In Figure 12 we also plot the

prediction at 300 ˚C $C_p = 2.7 \cdot 10^{-10}$ and m_p= 3.89 [5]. An estimate for 500 ˚C is also done by assuming the same temperature factor for n_p (3.3/4) and $C_p = 500/7.5$ as for RCC-MRx. These fatigue data give a much better agreement with test data. Other sources for the under-predicting the crack growth rate are: the higher ΔT at the inner surface and crack interaction in the test.

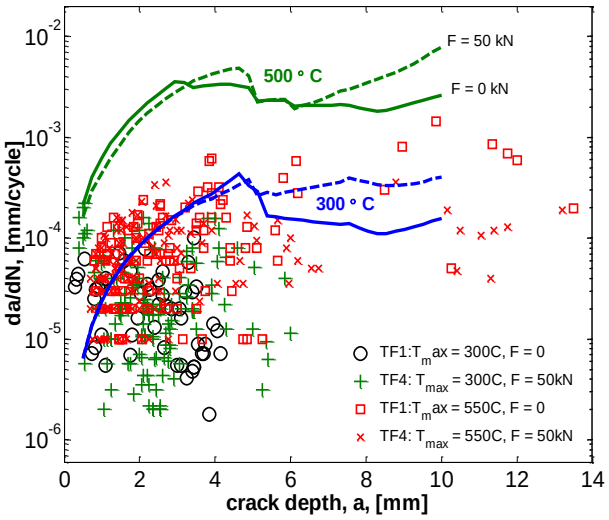

Figure 11 Computed crack growth rate vs. crack depth at 300 and 550 C and experimental data TF1, TF4, TFR1 and TFR2

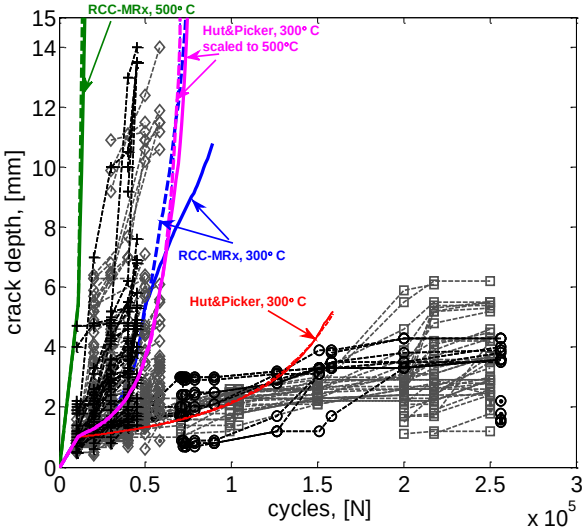

Figure 12 Computed crack depth. vs number of cycles with a0 = 1mm and 2.5 mm at 300 and 550 C RCC-MRx data and Huthmann& Picker and experimental data

Conclusion

We have presented experimental and computed data for a 316L steel pipe heated to 300 and 550 ºC and cooled by room temperature water shocks with no axial load and small axial load. The cracking is initiated as a network of surface cracks where some crack become dominant and propagates. From experimental data we conclude that the crack growth rate is significantly higher when the temperature is increased and that a small axial load increases significantly number of circumferential cracks and switch the dominant cracks from axial to circumferential. An accurate prediction of the crack growth requires an elasto-plastic analysis and that the crack aspect ratio increases with crack depth. The increased crack growth rate at the higher temperature is caused by the higher stress intensity factor as an increase of the propagation rate from the material data. The agreement with the data is sensitive to the assumed Paris law parameters. The RCC-MRx data gives a conservative estimate whereas lower literature data give very good agreement.

References

[1] Paffumi E., Nilsson K-F, Taylor N., Hurst R. and Bache M. R., Cracks initiation, propagation and arrest in 316L model pipe components under thermal fatigue, *J. ASTM International*, May 2005, Vol.2 No.5

[2] E. Paffumi, K.-F. Nilsson, N.G. Taylor, Simulation of Thermal Fatigue Damage in a 3156L Model Pipe Component, *Int. Journal of Pressure Vessel and Piping*, vol. 85, 798-813, 2008

[3] S. Marie et al. French RSE-M and RCC-MR code appendices for flaw analysis: Presentation of the fracture parameter calculation – Part III Cracked pipes, Int. J. Pressure Vessels Piping, 2007, 84, 614-658

[4] RCC-MRx Code 2010 Draft, AFCEN, France

[5] Huthmann H. and Picker C., Behaviour of short fatigue cracks in austenitic stainless steels literature review, European Commission, *Nuclear Science and Technology*, EUR 15186.

[6] W.J. Mills, L.A. James, Fatigue crack propagation behaviour of type 316 stainless steel at elevated temperature in a vacuum, *Int. J. Fatigue*, 1, 1988,, 33-36.

[7] H. Riedel, *Fracture at High Temperatures*, 1987, Materials Research and Engineering, Springer Verlag, Berlin